J. Fluid Mech. (2023), *vol*. 956, A19, doi:10.1017/jfm.2023.25

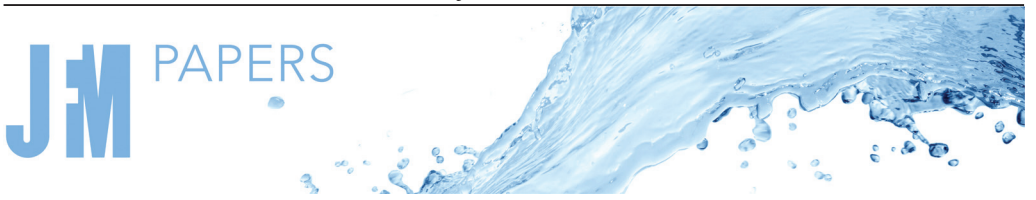

High humidity enhances the evaporation of non-aqueous volatile sprays

Mogeng Li[1],†, **Detlef Lohse**[1],[2] **and Sander G. Huisman**[1],†

[1]Physics of Fluids Group, Max Planck Center for Complex Fluid Dynamics, J. M. Burgers Center for Fluid Dynamics, Department of Science and Technology, University of Twente, 7500AE Enschede, The Netherlands

[2]Max Planck Institute for Dynamics and Self-Organisation, 37077 Göttingen, Germany

(Received 27 July 2022; revised 20 November 2022; accepted 3 January 2023)

We experimentally investigate the evaporation of very volatile liquid droplets (Novec 7000 Engineered Fluid, chemical name hydrofluoroethers HFE-7000) in a turbulent spray. Droplets with diameters of the order of a few micrometres are produced by a spray nozzle and then injected into a purpose-built enclosed dodecahedral chamber filled with air containing various amounts of water vapour. The ambient temperature and relative humidity in the chamber are carefully controlled. We observe water condensation on the rapidly evaporating droplet, both for the spray and for a single acoustically levitated millimetric Novec 7000 droplet. We further examine the effect of humidity, and reveal that a more humid environment leads to faster evaporation of the volatile liquid, as well as more water condensation. This is explained by the much larger latent heat of water as compared with that of Novec 7000. We extend an analytical model based on Fick's law to quantitatively account for the data.

Key words: condensation/evaporation, aerosols/atomization, drops

1. Introduction

Evaporation of volatile sprays plays an important role in many practical applications, such as fuel injection for combustion and spray cooling. For a single droplet in a quiescent environment, assuming that the evaporation process is limited by the diffusion of the vapour layer, the droplet diameter can be described by the so-called d^2-law, where d denotes the droplet diameter (Langmuir 1918). The evaporation rate depends on many flow parameters and material properties, including the ambient temperature, the vapour

† Email addresses for correspondence: mogeng.li@utwente.nl, s.g.huisman@utwente.nl

pressure of the liquid, as well as the vapour concentration in the ambient environment. The evaporating droplet cools down due to its latent heat. Its temperature asymptotes to a constant value lower than the ambient temperature, which can be evaluated by balancing the absorption of latent heat in the liquid-to-gas phase transition with the heat transfer between the droplet and the surrounding air (Dalla Barba, Wang & Picano 2021). When a stationary droplet is exposed to an external turbulent flow, the turbulent convection will accelerate the transport of vapour away from the droplet, resulting in larger concentration gradients and thus in higher evaporation rates and shorter droplet lifetimes (Birouk & Gökalp 2006). On the other hand, when the droplet itself is moved by the turbulence, it may pass through regions with different vapour concentrations along its trajectory, and the instantaneous droplet evaporation rate is affected accordingly.

When a multicomponent droplet is considered, a few complications are introduced alongside. Different components evaporate at different rates, creating a concentration gradient in the liquid phase. The evaporation process is affected not only by the vapour diffusion rate in air as in the single-component scenario, but also by the interspecies diffusion of different vapours, multicomponent phase equilibrium relations (typically Raoult's law) and the diffusion and convection in the liquid phase (Sirignano 2010). The vaporisation of multicomponent droplets has been studied extensively in the context of combustion, especially in the scenario of a mixture of various fuels vaporising at an elevated temperature (Daïf *et al.* 1998; Ra & Reitz 2009; Promvongsa *et al.* 2017).

For a non-aqueous single-component droplet evaporating in a humid environment at room temperature, it has been observed that water vapour in the ambient air condenses on the evaporating droplet, forming a multicomponent droplet (Law, Xiong & Wang 1987; Marié *et al.* 2014), provided that the evaporative cooling process can lead to a droplet temperature low enough to saturate the water vapour. The size evolution of the multicomponent droplet in these studies was measured by direct imaging and digital holography, respectively, and described by an analytical model, where the two mass transfer equations are coupled through a heat transfer equation.

In this study, we further demonstrate that the ambient humidity affects the evaporation of a non-aqueous volatile droplet through the condensation process. The experimentally measured water condensation droplet size is compared with model predictions, and the effect of turbulent convection is discussed with an analytical model.

The paper is organised as follows: we first provide details of the experimental method in § 2. Measurements of droplet sizes in a spray and the analytical model are covered in § 3. The effect of ambient turbulence is further discussed in § 4 and finally the observation of a single millimetric droplet evaporating in an acoustic levitator is detailed in § 5. The paper ends with conclusions and an outlook.

2. Experiment set-up

A dodecahedral chamber has been constructed to investigate this problem. A schematic of the set-up is shown in figure 1(*a*). The chamber has 12 pentagonal faces with a side length of 30 cm, resulting in a volume of ≈210 l. To generate a homogeneous isotropic turbulent flow field in the centre of the dodecahedron, 20 identical axial fans are mounted at the vertices and driven by the same DC power. All fans are rigged to simultaneously blow into the centre of the dodecahedron. The chamber is capable of achieving 'ambient turbulence' or 'quiescent' conditions by switching these axial fans on or off. The chamber is not hermetic and the pressure remains around 1 atm during operation. The temperature in the chamber can be regulated through the two heating/cooling plates on the side, which are connected to an external heater/cooler Julabo FP51-SL capable of achieving a temperature

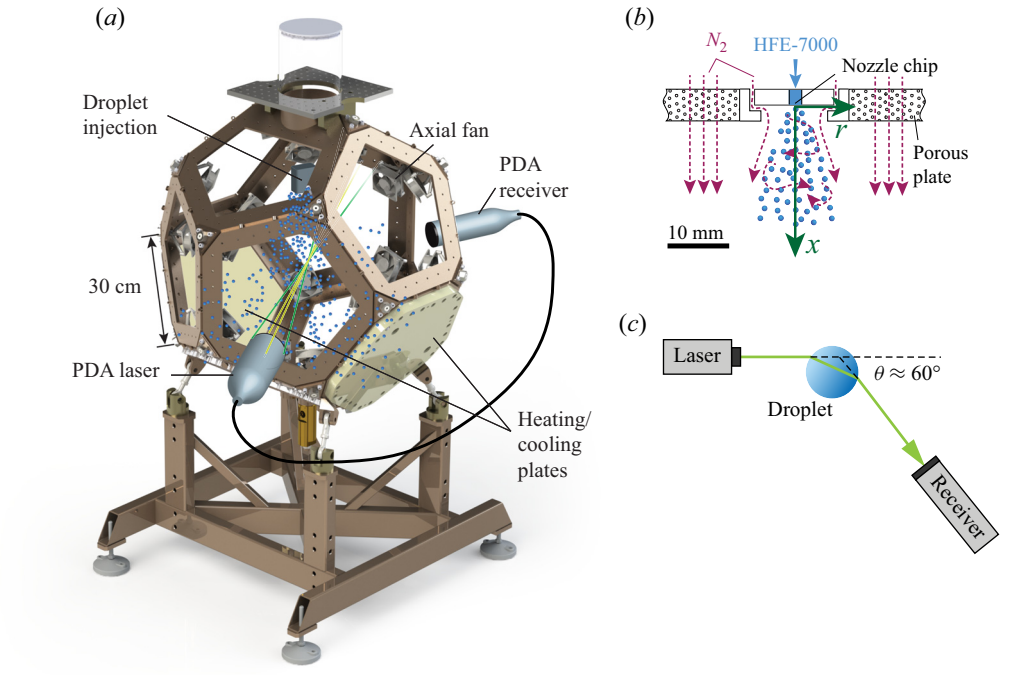

Figure 1. (*a*) The dodecahedral chamber with PDA measurement system. The chamber is enclosed by 12 pentagonal transparent acrylic window panels (not shown in the drawing). The droplets are injected through a nozzle chip from the top of the chamber. (*b*) Schematic showing a close-up view of the nozzle provided by Medspray. The nozzle chip contains 90 holes with a diameter of 4.5 μm. (*c*) Laser optical path, with the first-order refraction mode captured by the receiver. The droplets in all panels are not shown to scale.

range of −30–80 °C. The relative humidity (RH) can also be controlled within a range between 20 % and 100 %, by either injecting water using an air humidifier or removing excess moisture by pumping the air through an in-line dryer filled with desiccants. To avoid any disturbance to the flow field, RH is adjusted beforehand and it remains relatively unchanged during each measurement thanks to the enclosed nature of the chamber. The temperature, RH and atmospheric pressure are sampled using a BME280 sensor with an in-house built Arduino data acquisition system.

The nozzle used to generate the spray is provided by Medspray. As illustrated in figure 1(*b*), droplets are formed at the nozzle chip driven by a syringe pump, and carried downstream by a 15 l min^{-1} (approximately 7 m s^{-1} at the nozzle chip) co-flow to prevent coalescence. We choose to use Novec 7000 Engineered Fluid (chemical name hydrofluoroethers HFE-7000, hereinafter referred to as 'HFE-7000' in short) manufactured by 3M (3M 2021), and also characterised by Rausch *et al.* (2015). In essence, HFE-7000 is extremely volatile, with a very high saturation vapour pressure of 52.7 kPa at 20 °C, and it is relatively harmless to the ozone layer and the acrylic windows of the dodecahedron.

The droplet diameters are measured using a Dantec two-component phase Doppler anemometry (PDA) system with a 112 mm FiberFlow probe. Schematics of the set-up and the optical arrangement are shown in figures 1(*a*) and 1(*c*). The receiving probe is positioned at an off-axis angle of $\theta \approx 60°$, where the first-order refraction is the dominant mode. Details of the measurement principle can be found in Albrecht *et al.* (2013). Essentially, light scattered by a droplet in the measurement volume, which is

the intersection of two focused laser beams, is captured by two or more receivers at slightly different angles. Each detector converts the optical signal into a Doppler burst, the frequency of which is linearly proportional to the droplet velocity, and the droplet size is directly inferred from the phase difference in the signals. The PDA set-up is equipped with a 3-detector system, which can largely prevent phase ambiguity, and cover a wide particle size range without sacrificing the resolution. The measurable size range is 0.5–137.4 μm. The measurement volume is fixed at the centre of the dodecahedron, while the spray nozzle is traversed to obtain axial and radial profiles. At each measurement location, the PDA signal is sampled for 30 s. The concentration of HFE-7000 vapour in the ambient environment is considered negligible, as during each run less than 2 ml of the liquid is injected, whereas 650 ml is needed to saturate the entire volume of the dodecahedron.

3. Experimental results on droplet evaporation in a spray

We first explore the change in the average droplet diameter along the centreline (x coordinate) of the spray jet in a quiescent ambient environment, where the 20 turbulence generating axial fans are off. Figures 2(a) and 2(b) show the probability density distributions (p.d.f.) of the measured droplet diameters for the ambient RH cases of RH = 20 % and RH = 100 %, respectively. Close to the nozzle, the distribution exhibits a broad peak centred around $d = 6$ μm. Further away from the nozzle, as shown by the lines with a lighter shade, the magnitude of this peak reduces while a second peak emerges at a much smaller size, $d = 2$–3 μm. This peak at small diameters keeps growing with increasing x, eventually exceeding the magnitude of the first peak. We believe that the emergence of the second peak at much smaller diameters is a result of water in the ambient air condensing on the rapidly evaporating HFE-7000 droplets. An analytical model is extended based on the work of Marié *et al.* (2014) and Tonini & Cossali (2015), taking the immiscibility between HFE-7000 and water into consideration. Details of the model are summarised in Appendix A. Assuming that the droplets measured at $x = 20$ mm contain HFE-7000 only, we use the recorded size distribution at this location as the initial condition, and final condensed water droplet size distribution can be predicted by the model (Appendix A) and is shown by the black lines. The peak at $d \approx 2$ μm in the predicted condensed water droplet size directly results from the peak at $d_0 \approx 6$ μm in the initial size distribution. Indeed, the measured size distribution can be well captured by the model prediction. Note that, at this stage, we consider a single, stationary droplet, not affected by the vapour field of neighbouring droplets and the evaporation–condensation rate is limited by the diffusion of the vapour film around the droplet. Although many effects, including the turbulent convection (Birouk & Gökalp 2006; Méès *et al.* 2020; Dodd *et al.* 2021) and the sheltering in clusters of droplets (Villermaux *et al.* 2017; Sahu, Hardalupas & Taylor 2018; Dodd *et al.* 2021), are not taken into consideration, the modelled remaining water droplet size distribution still has a good agreement with the measurements.

We consider the HFE-7000 component fully evaporated in any measured droplet with a diameter smaller than a certain threshold d_{thr}. Thus, a ratio α can be defined as the ratio between the number of droplets with $d < d_{thr}$ and the total number of droplets measured at the same location. The threshold is chosen as $d_{thr} = 4.7$ μm, which is larger than 99.5 % of the predicted remaining water droplet size in the RH = 100 % case (black line in figure 2b). Note that the same value for d_{thr} is used across all RH cases for consistency, although more droplets that still contain liquid HFE-7000 will be mistaken as remaining water droplets in low ambient RH cases. The spatial variation of α at a range of ambient relative humidities is depicted in figure 3. In both axial and radial directions, α

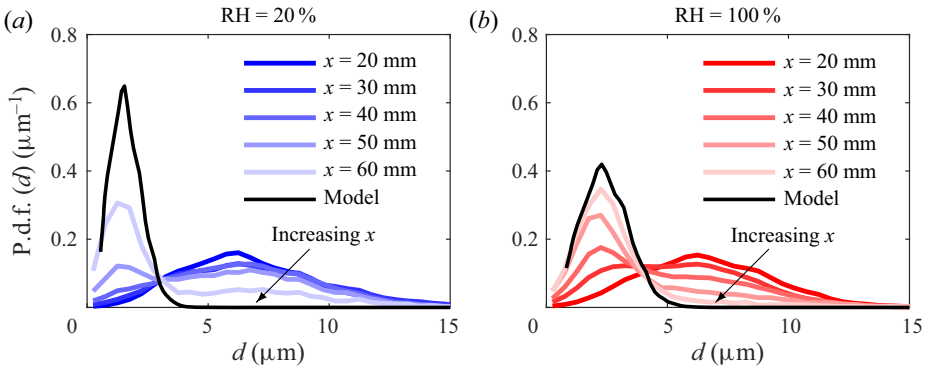

Figure 2. Droplet size distribution at (*a*) RH = 20 % and (*b*) RH = 100 % in a quiescent ambient environment. From dark to light, the line colour indicates an increasing distance x from the nozzle along the centreline, ranging from $x = 20$ to $x = 60$ mm. The solid black line is the predicted condensed water droplet size distribution based on the analytical model of Appendix A, valid for large distances x.

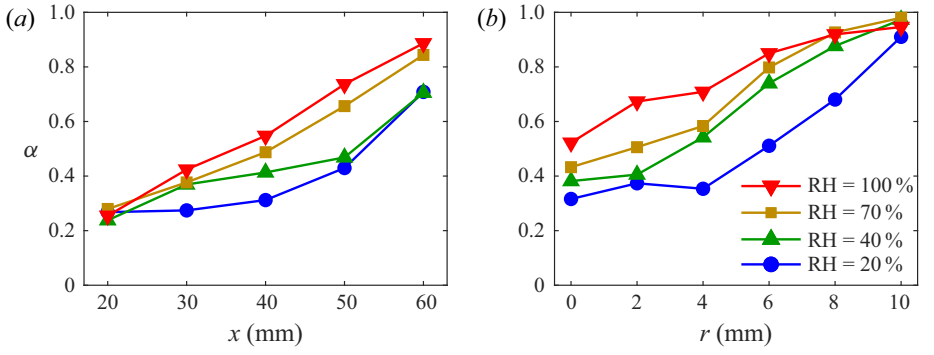

Figure 3. The fraction α of remaining water droplets among the total number of measured droplets along (*a*) the axial direction ($r = 0$) and (*b*) the radial direction ($x = 40$ mm) in a quiescent ambient environment.

increases with increasing distance from the nozzle, confirming the sheltering effect in the jet (Villermaux *et al.* 2017; Wang, Dalla Barba & Picano 2021). Furthermore, we observe a strong dependence of α on RH: at the same location, α increases with RH, indicating that HFE-7000 evaporates faster in a more humid environment.

The observation can be explained by inspecting the modelled single droplet behaviour. As shown in figures 4(*a*) and 4(*b*), indeed, the predicted lifetime of a HFE-7000 droplet at RH = 100 % is around 40 % shorter than that at RH = 20 %. The reason behind this higher evaporation rate lies in the latent heat and the resulting temperature. As shown in figure 4(*e*,*f*), when the HFE-7000 droplet is exposed to ambient air, its temperature rapidly decreases as a result of the latent heat absorbed during the liquid-to-gas phase transition. This phenomenon is also known as 'evaporative cooling'. The cold droplet cools down its surrounding gas film, reducing the saturation vapour mass fraction of water it carries. As a consequence, the local RH will increase, and once it exceeds 1, the water vapour becomes over-saturated and will start condensing on the surface of the droplet. At a high ambient RH (figure 4*d*), the rate of water condensation significantly increases and the latent heat released in the process heats up the droplet to a higher temperature, therefore the HFE-7000 component will evaporate at a higher temperature and a faster rate. Furthermore, high RH environment leads to a larger water core, giving rise to a

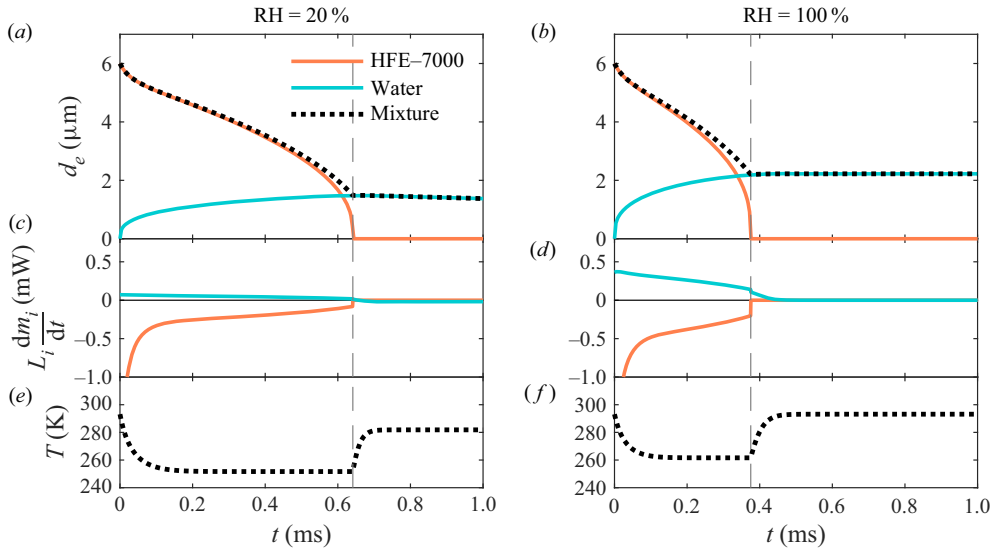

Figure 4. Model prediction of (*a*,*b*) the equivalent droplet diameter of composing liquids, (*c*,*d*) the rate of latent heat absorbed/released by the droplet and (*e*,*f*) the droplet temperature as a function of time at (*a*,*c*,*e*) RH = 20 % and (*b*,*d*,*f*) RH = 100 %. The droplet initially contains only HFE-7000 and the ambient temperature is $T_\infty = 20\,^\circ$C (293.15 K), and the initial diameter is set to a typical size of $d_0 = 6$ μm.

higher surface-to-volume ratio of the HFE-7000 component, which also accelerates the evaporation.

4. Effect of turbulence

In this section, we discuss the effect of ambient turbulence on the observed evaporation–condensation process. The effect of turbulence is usually modelled through Ranz–Marshall correlations, and is characterised by a single non-dimensional parameter $Re_d \equiv dU_r/\nu$, which is the droplet Reynolds number based on d, the diameter, U_r, the velocity relative to the surrounding gas, and ν, the kinematic viscosity of air. Since the droplet diameter d changes during evaporation, we represent the level of turbulence using $Re_{d_0} \equiv d_0 U_r/\nu$, the droplet Reynolds number based on the initial diameter and assume the relative velocity U_r remains constant. In the present experiments, the relative velocity is not measured, nevertheless, Re_{d_0} is estimated to be well below 10 considering the small size of the droplets. Figure 5 compares t_{evap}, the time required for HFE-7000 to fully evaporate, and d_w, the water condensation droplet size at various Re_{d_0} values. Overall, t_{evap} reduces with increasing ambient RH. For a given RH, t_{evap} is also found to be smaller at a higher Re_{d_0}, as the mass and heat exchange is enhanced by turbulent convection. In the limit of extremely large Re_{d_0} which is not practical for the current configuration, a power law relationship $t_{evap} \propto Re_{d_0}^{-2/5}$ emerges as a consequence of (A14*a*). Interestingly, despite the large variation in t_{evap}, very little change is observed in the final condensed water droplet size d_w, as shown in figure 5(*b*). This suggests that as turbulent convection enhances the evaporation, the rate of condensation is also increased almost proportionally: similar to its effect in reducing the local HFE-7000 vapour concentration by advecting the HFE-7000 vapour away from the droplet, the turbulence also serves to replenish the droplet surface with over-saturated humid air. This result also explains why even the

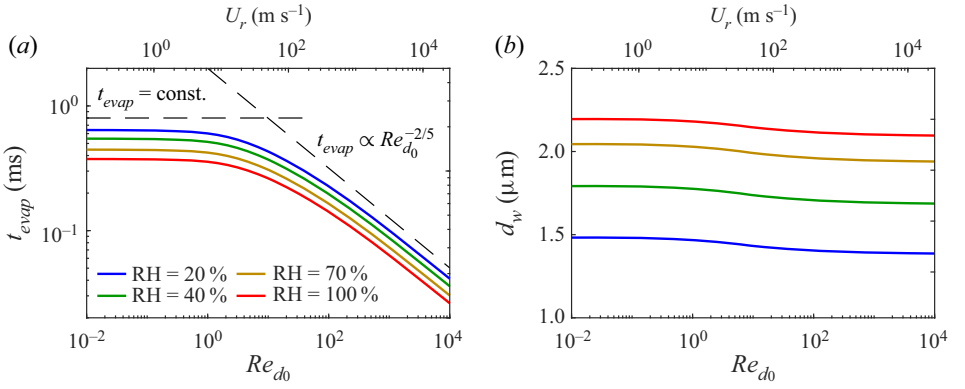

Figure 5. Model prediction at a range of droplet Reynolds numbers, Re_{d_0}. (*a*) The time required for the HFE-7000 component to fully evaporate t_{evap}, and (*b*) the diameter of condensed water droplets d_w. All results are for a HFE-7000 droplet with an initial diameter of $d_0 = 6$ μm at an ambient temperature of $T_\infty = 20\,^\circ$C (293.15 K).

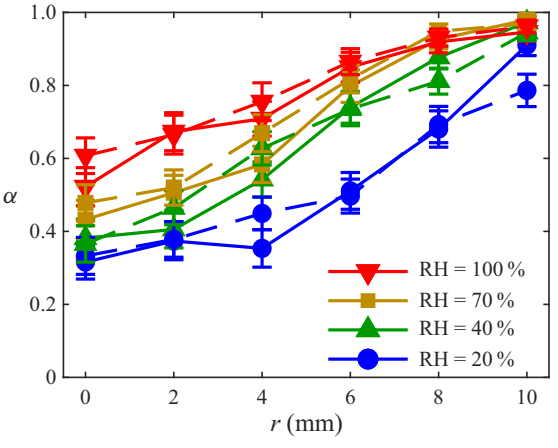

Figure 6. The fraction of remaining water droplets among the total number of measured droplets with (dashed line) and without (solid line) the presence of ambient turbulence. The error bars show the standard deviation of the mean estimated using a bootstrapping approach.

diffusion-limited model can produce a remaining water droplet size distribution with a high level of agreement with the experimental data.

Experimentally, the ambient turbulence is generated by the 20 axial fans mounted in the dodecahedral chamber. We would like to point out that the spray is already at a turbulent state even though the surrounding air in the dodecahedral chamber is under quiescent conditions. The ambient turbulence is, in fact, acting on an already turbulent jet spray. Figure 6 compares α, the proportion of the condensed water droplets at a number of measurement locations along the radial direction with quiescent and turbulent ambient conditions. The data with ambient turbulence display a similar trend of increasing α with increasing x and RH, and there is no major difference from the quiescent case.

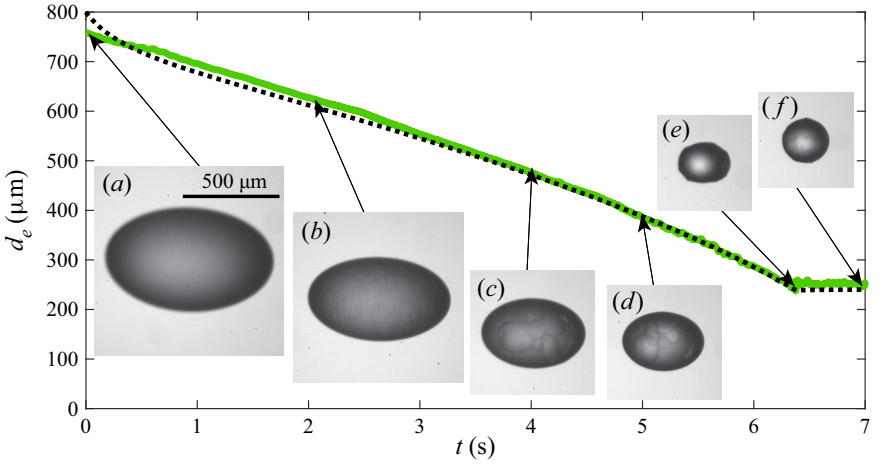

Figure 7. Temporal evolution of the droplet equivalent diameter d_e. The solid green line is measured from droplet images, and the dotted black line is computed from the model, with $Re_{d_0} = 10$ selected to best replicate the experimental observation. Insets (*a–f*) are droplet images at time instances marked by the arrows. The scale bar in (*a*) holds for all images.

5. Observations of a single droplet

In this section, we provide further experimental evidence of the water condensation that accompanies the rapid vaporisation process by directly imaging a single, millimetre-scale HFE-7000 droplet in an acoustic levitator. The droplet is imaged using a Photron Nova S12 high-speed camera with a Navitar 12× lens at 500 Hz.

Snapshots of the multi-component droplet are shown in figure 7. The moment the droplet is injected in the acoustic levitator is denoted as $t = 0$. At $t = 2.0$ s (figure 7*b*), small water droplets with a diameter around 20 μm distribute within the HFE-7000 drop. Carried by the internal flow, which is caused by the internal circulation as well as the acoustic field, these water droplets move in the HFE-7000 drop, collide and coalesce into larger clusters as clearly visible in figures 7(*c*) and 7(*d*). These clusters have complex, non-spherical shapes. When the amount of remaining liquid HFE-7000 is not sufficient to wet the entire surface of the water clusters and fill the grooves, these water clusters are exposed and the drop exhibits an irregular shape with protrusions (figure 7*e*). After this transient phase, only a single-composition water droplet remains (figure 7*f*). It has a spherical shape, as a result of the increase in the surface tension with HFE-7000 being replaced by water at the droplet surface. These observations clearly validate the modelling assumption that the water condensation forms an inclusion within a HFE-7000 shell (see figure 8*b*), and the droplet surface contains predominantly only HFE-7000. Supplementary movie 1 available at https://doi.org/10.1017/jfm.2023.25 shows the entire evaporation–condensation process. Note that for a typical droplet in the spray, the diameter is less than 1 % of the acoustic levitated drop diameter here, and it shape is more spherical even in the multi-component stage because of the much smaller Weber number.

The droplet has an oblate ellipsoidal shape as a result of levitation by the acoustic field (Yarin *et al.* 1999; Al Zaitone 2018). The major and minor axis lengths d_a and d_b are measured from the image, and the equivalent diameter d_e is calculated as $d_e = (d_a^2 d_b)^{1/3}$. The ratio d_b/d_a is approximately 0.6 until HFE-7000 is fully evaporated. The evaporation time of a spherical droplet with the same equivalent diameter gives a reasonable approximation of the ellipsoidal case (Tonini & Cossali 2016, 2019).

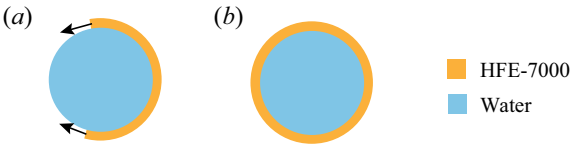

Figure 8. (*a*) Low-surface-tension component (HFE-7000) wraps around the high-surface-tension water core, driven by the difference in surface tension. (*b*) The wrapping process is complete and HFE-7000 forms a shell around the water core.

The measured diameter variation matches well with the model prediction at $Re_{d_0} = 10$, which corresponds to a relative velocity of $U_r \approx 0.2$ m s^{-1}.

6. Conclusions and outlook

In this work, we experimentally observe an interesting evaporation–condensation process of a volatile spray in humid air. The evaporation of HFE-7000 and the condensation of water can be described by an analytical model based on Fick's law. The immiscibility between HFE-7000 and water is taken into consideration, through a model of the condensation water core contained in the HFE-7000 droplet, as corroborated by the direct imaging of a single droplet in an acoustic levitator. The analytical model also reveals that, in a more humid environment, the droplet temperature is higher because more latent heat is released with a higher rate of water condensation under such conditions, confirming the faster HFE-7000 evaporation rate found in experiments.

In future works, the detailed physics of the water condensation process in the single levitated (or sessile) droplet should be explored: how the condensed water migrates to the interior of the droplet remains an open question. Further, exploring other liquid pairs with high miscibility and different volatilities is also of interest, because they can result in evaporation rates very different from the current findings.

Supplementary movie. Supplementary movie is available at https://doi.org/10.1017/jfm.2023.25.

Acknowledgements. We acknowledge W. Nijdam and S. van der Vegte from Medspray for providing the nozzles and technical support during the project. We would also like to thank U. Sen for the single levitated droplet measurements, G.-W. Bruggert for the design of the dodecahedron, D. van Gils for developing the Arduino data acquisition system, G. Mentink and R. Nauta for building the linear traverse and axial fan power supply, M. Bos and T. Zijlstra for technical support and L. Bourouiba, A. Prosperetti and C. Sun for discussion.

Funding. This work was funded by the Netherlands Organisation for Health Research and Development (ZonMW), project number 10430012010022: 'Measuring, understanding and reducing respiratory droplet spreading' and the Netherlands Organisation for Scientific Research (NWO) through the Multiscale Catalytic Energy Conversion (MCEC) research centre.

Declaration of interests. The authors report no conflict of interest.

Author ORCIDs.
Mogeng Li https://orcid.org/0000-0002-9875-6468;
Detlef Lohse https://orcid.org/0000-0003-4138-2255;
Sander G. Huisman https://orcid.org/0000-0003-3790-9886.

Appendix A. Details of the evaporation–condensation analytical model

The evaporation–condensation model used in this paper is developed based on the works of Law & Binark (1979), Law *et al.* (1987) and Marié *et al.* (2014), and the Fick's

law-based multicomponent droplet vaporisation model (Tonini & Cossali 2015), with the immiscibility of the HFE-7000–water system taken into consideration. Details of the model are summarised below.

We consider that the gas film surrounding the droplet is spherically symmetric. The evaporation–condensation process is dictated by the vapour diffusion, and the inter-species vapour diffusion is neglected. The droplet is assumed to have a uniform temperature. Following Tonini & Cossali (2015), we describe the multicomponent system using two mass transfer equations and a heat transfer equation of the two-component droplet

$$\frac{\mathrm{d}m_1}{\mathrm{d}t} = \dot{m}_T \frac{Y_1^s - Y_1^\infty \exp\left(\dfrac{\dot{m}_T}{2\pi\rho^g d D_1}\right)}{1 - \exp\left(\dfrac{\dot{m}_T}{2\pi\rho^g d D_1}\right)} \frac{Sh_1}{2} \tag{A1a}$$

$$\frac{\mathrm{d}m_2}{\mathrm{d}t} = \dot{m}_T \frac{Y_2^s - Y_2^\infty \exp\left(\dfrac{\dot{m}_T}{2\pi\rho^g d D_2}\right)}{1 - \exp\left(\dfrac{\dot{m}_T}{2\pi\rho^g d D_2}\right)} \frac{Sh_2}{2} \tag{A1b}$$

$$(m_1 + m_2)\, c_p^d \frac{\mathrm{d}T^d}{\mathrm{d}t} = \pi d \lambda^g Nu \frac{\log(1 + B_T)}{B_T} \left(T^\infty - T^d\right) + L_1 \frac{\mathrm{d}m_1}{\mathrm{d}t} + L_2 \frac{\mathrm{d}m_2}{\mathrm{d}t}, \tag{A1c}$$

where m is the liquid mass, Y the vapour mass fraction, d the droplet diameter, ρ the density, D the diffusion coefficient in air, c_p the specific heat capacity, T the temperature, λ the thermal conductivity, L the specific latent heat of vaporisation and B_T the Spalding number of heat transfer (A11). Subscripts 1 and 2 refer to the HFE-7000 and water components, respectively, and a refers to air. Superscript ∞ indicates ambient conditions, d refers to the droplet, s refers to droplet surface and g refers to the vapour gas film around the droplet. The droplet heat capacity c_p^d is computed as the weighted average of that of individual components, and the gas film heat capacity c_p^g and thermal conductivity λ^g are approximated by those of air. The temperature dependence of D, L, c_p and λ of a single component is neglected. Here, $\dot{m}_T$ is the total change rate of the droplet mass without convection correction, which by definition is

$$\dot{m}_T = \frac{\mathrm{d}m_1}{\mathrm{d}t}\frac{2}{Sh_1} + \frac{\mathrm{d}m_2}{\mathrm{d}t}\frac{2}{Sh_2} \tag{A2}$$

and can be found implicitly from the nonlinear equation

$$\frac{Y_1^\infty - Y_1^s}{\exp\left(\dfrac{\dot{m}_T}{2\pi\rho^g d D_1}\right) - 1} + \frac{Y_2^\infty - Y_2^s}{\exp\left(\dfrac{\dot{m}_T}{2\pi\rho^g d D_2}\right) - 1} = 1 - Y_1^\infty - Y_2^\infty. \tag{A3}$$

The vapour mass fraction at the droplet surface can be expressed as

$$Y_1^s = \frac{X_1 P_{sat1}^s M_1}{X_1 P_{sat1}^s M_1 + X_2 P_{sat2}^s M_2 + \left(P^\infty - X_1 P_{sat1}^s - X_2 P_{sat2}^s\right) M_a}, \tag{A4a}$$

$$Y_2^s = \frac{X_2 P_{sat2}^s M_2}{X_1 P_{sat1}^s M_1 + X_2 P_{sat2}^s M_2 + \left(P^\infty - X_1 P_{sat1}^s - X_2 P_{sat2}^s\right) M_a}, \tag{A4b}$$

where P_{sat} is the saturated vapour pressure, P^∞ is the ambient pressure, M is molecular weight and X_1 and X_2 are the surface area fractions of the HFE-7000 and water

components, respectively. Here, P_{sat} is dependent on the local temperature, and can be evaluated from the empirical relations as

$$\log\left(P_{sat1}\right) = 22.978 - \frac{3548.6}{T} \tag{A5}$$

for HFE-7000 (3M 2021), and

$$\log_{10}\left(P_{sat2}\right) = A - \frac{B}{T + C} \tag{A6}$$

for water, with coefficients $A = 9.6543$, $B = 1435.264$ and $C = -64.848$ (Stull 1947). The unit of P_{sat} is Pa, and T is in K.

Unlike typical fuels, which are considered in the model of Sirignano (2010), and also commonly used in the combustion community, water and HFE-7000 have very low solubility in each other ($\lesssim$60 ppmw, 3M 2021). Therefore, the assumption that liquid in the droplet is fully mixed is not applicable to our system. HFE-7000 has a very low surface tension of 12.33 mN m^{-1} at room temperature (Rausch *et al.* 2015) compared with 72 mN m^{-1} for water, so it will wrap around the water droplet core, driven by the surface tension, as shown in figure 8(*a*). For a water core with a diameter of 2 μm, the time required for the HFE-7000 film to completely wrap around it is estimated to be 30 ns (Koldeweij *et al.* 2019), which is much shorter than the droplet lifetime. Therefore, we consider a 'shell' model of the evaporating droplet as depicted in figure 8(*b*). In this scenario, the surface area fractions are $X_1 = 1$ and $X_2 = 0$. When HFE-7000 is fully evaporated, the water core will be fully exposed and the surface area fractions therefore become $X_1 = 0$ and $X_2 = 1$. Note that the assumption of $X_1 = 0$ in the shell model introduces a bias towards water condensation, resulting in an overestimation of the final condensation water droplet size. However, if the other extreme assumption of $X_1 = 1$ and $X_2 = 1$ (water vapour is fully saturated at the surface) is used instead, for the range of RH considered in this work, there is less than 10 % change in the condensation water droplet size, and the difference decreases with increasing RH.

The reference mass fractions and temperature in the gas film are estimated using the so-called 1/3 law (Hubbard, Denny & Mills 1975)

$$Y_1^r = \tfrac{2}{3}Y_1^s + \tfrac{1}{3}Y_1^\infty, \tag{A7a}$$

$$Y_2^r = \tfrac{2}{3}Y_2^s + \tfrac{1}{3}Y_2^\infty, \tag{A7b}$$

$$T^r = \tfrac{2}{3}T^s + \tfrac{1}{3}T^\infty. \tag{A7c}$$

Note that $T^s = T^d$ according to the assumption of uniform droplet temperature.

The gas film density is computed from a weighted harmonic mean of the compositions

$$\rho^g = \frac{1}{\dfrac{Y_1^r}{\rho_1} + \dfrac{Y_2^r}{\rho_2} + \dfrac{1 - Y_1^r - Y_2^r}{\rho_a}}, \tag{A8}$$

where the gas density of each component is computed using the ideal gas law at the reference temperature T_r

$$\rho_i = \frac{P^\infty M_i}{RT^r}, \quad i = 1, 2, a. \tag{A9}$$

The Spalding number of mass transfer is a non-dimensional thermodynamics parameter measuring the ratio of drive towards vaporisation as compared with resistance to

vaporisation (Abramzon & Sirignano 1989)

$$B_M = \frac{Y_1^s - Y_1^\infty + Y_2^s - Y_2^\infty}{1 - Y_1^s - Y_2^s}, \tag{A10}$$

and the Spalding number of heat transfer B_T can be linked to B_M through (Marié *et al.* 2014)

$$\log\left(1 + B_T\right) = \frac{c_p^g D^g \rho^g}{\lambda^g} \log\left(1 + B_M\right). \tag{A11}$$

Here, D^g is computed from a weighted average of the two components

$$D^g = \frac{Y_1^r D_1 + Y_2^r D_2}{Y_1^r + Y_2^r}. \tag{A12}$$

Finally, the effect of turbulent convection is incorporated using the so-called 'film theory', which assumes that the resistance to heat or mass exchange between a surface and a gas flow may be modelled by introducing the concept of a surrounding gas film (Frank-Kamenetski 1969; Abramzon & Sirignano 1989). The Sherwood and Nusselt numbers can be expressed as (Abramzon & Sirignano 1989)

$$Sh_1 = 2 + \frac{Sh_{01} - 2}{F(B_M)}, \tag{A13a}$$

$$Sh_2 = 2 + \frac{Sh_{02} - 2}{F(B_M)}, \tag{A13b}$$

$$Nu = 2 + \frac{Nu_0 - 2}{F(B_T)}, \tag{A13c}$$

where Sh_0 is the Sherwood number and Nu_0 the Nusselt number for a non-vaporising sphere (Abramzon & Sirignano 1989)

$$Sh_{01} = 1 + \left(1 + Re_d\, Sc_1^g\right)^{1/3} \max\left(1, Re_d^{0.077}\right), \tag{A14a}$$

$$Sh_{02} = 1 + \left(1 + Re_d\, Sc_2^g\right)^{1/3} \max\left(1, Re_d^{0.077}\right), \tag{A14b}$$

$$Nu_0 = 1 + \left(1 + Re_d\, Pr^g\right)^{1/3} \max\left(1, Re_d^{0.077}\right), \tag{A14c}$$

$$\text{for } Re_d \leqslant 5, \tag{A14d}$$

with

$$Sc_1^g = \frac{\mu^g}{D_1 \rho^g}, \quad Sc_2^g = \frac{\mu^g}{D_2 \rho^g}, \quad Pr^g = \frac{\mu^g c_p^g}{\lambda^g}, \tag{A15a–c}$$

where μ^g is the dynamic viscosity of the gas film around the droplet, and it is approximated by that of air. The term $F(B)$ represents the relative change of the gas film thickness due to the Stefan flow around the droplet, which is given by (Abramzon & Sirignano 1989)

$$F(B) = (1 + B)^{0.7} \frac{\log(1 + B)}{B}, \quad B = B_M, B_T,$$
$$\text{for } 0 \leqslant B_T,\ B_M \leqslant 20,\ 1 \leqslant Pr,\ Sc \leqslant 3. \tag{A16}$$

References

3M 2021 Novec^{TM} 7000 Engineered Fluid technical data sheet. Available at: https://multimedia.3m.com/mws/media/121372O/3m-novec-7000-engineered-fluid-tds.pdf.

Abramzon, B. & Sirignano, W.A. 1989 Droplet vaporization model for spray combustion calculations. *Intl J. Heat Mass Transfer* **32** (9), 1605–1618.

Al Zaitone, B. 2018 Oblate spheroidal droplet evaporation in an acoustic levitator. *Intl J. Heat Mass Transfer* **126**, 164–172.

Albrecht, H.-E., Damaschke, N., Borys, M. & Tropea, C. 2013 *Laser Doppler and Phase Doppler Measurement Techniques*. Springer.

Birouk, M. & Gökalp, I. 2006 Current status of droplet evaporation in turbulent flows. *Prog. Energy Combust. Sci.* **32** (4), 408–423.

Daïf, A., Bouaziz, M., Chesneau, X. & Chérif, A.A. 1998 Comparison of multicomponent fuel droplet vaporization experiments in forced convection with the Sirignano model. *Exp. Therm. Fluid Sci.* **18** (4), 282–290.

Dalla Barba, F., Wang, J. & Picano, F. 2021 Revisiting D^2-law for the evaporation of dilute droplets. *Phys. Fluids* **33** (5), 051701.

Dodd, M.S., Mohaddes, D., Ferrante, A. & Ihme, M. 2021 Analysis of droplet evaporation in isotropic turbulence through droplet-resolved DNS. *Intl J. Heat Mass Transfer* **172**, 121157.

Frank-Kamenetski, D.A. 1969 *Diffusion and Heat Transfer in Chemical Kinetics*. Plenum.

Hubbard, G.L., Denny, V.E. & Mills, A.F. 1975 Droplet evaporation: effects of transients and variable properties. *Intl J. Heat Mass Transfer* **18** (9), 1003–1008.

Koldeweij, R.B.J., Van Capelleveen, B.F., Lohse, D. & Visser, C.W. 2019 Marangoni-driven spreading of miscible liquids in the binary pendant drop geometry. *Soft Matt.* **15** (42), 8525–8531.

Langmuir, I. 1918 The evaporation of small spheres. *Phys. Rev.* **12** (5), 368–370.

Law, C.K. & Binark, M. 1979 Fuel spray vaporization in humid environment. *Intl J. Heat Mass Transfer* **22** (7), 1009–1020.

Law, C.K., Xiong, T.Y. & Wang, C. 1987 Alcohol droplet vaporization in humid air. *Intl J. Heat Mass Transfer* **30** (7), 1435–1443.

Marié, J.-L., Grosjean, Na., Méès, L., Seifi, M., Fournier, C., Barbier, B. & Lance, M. 2014 Lagrangian measurements of the fast evaporation of falling diethyl ether droplets using in-line digital holography and a high-speed camera. *Exp. Fluids* **55** (4), 1–13.

Méès, L., Grosjean, N., Marié, J.-L. & Fournier, C. 2020 Statistical Lagrangian evaporation rate of droplets released in a homogeneous quasi-isotropic turbulence. *Phys. Rev. Fluids* **5** (11), 113602.

Promvongsa, J., Vallikul, P., Fungtammasan, B., Garo, A., Grehan, G. & Saengkaew, S. 2017 Multicomponent fuel droplet evaporation using 1D global rainbow technique. *Proc. Combust. Inst.* **36** (2), 2401–2408.

Ra, Y. & Reitz, R.D. 2009 A vaporization model for discrete multi-component fuel sprays. *Intl J. Multiphase Flow* **35** (2), 101–117.

Rausch, M.H., Kretschmer, L., Will, S., Leipertz, A. & Fröba, A.P. 2015 Density, surface tension, and kinematic viscosity of hydrofluoroethers HFE-7000, HFE-7100, HFE-7200, HFE-7300, and HFE-7500. *J. Chem. Engng Data* **60** (12), 3759–3765.

Sahu, S., Hardalupas, Y. & Taylor, A.M.K.P. 2018 Interaction of droplet dispersion and evaporation in a polydispersed spray. *J. Fluid Mech.* **846**, 37–81.

Sirignano, W.A. 2010 *Fluid Dynamics and Transport of Droplets and Sprays*. Cambridge University Press.

Stull, D.R. 1947 Vapor pressure of pure substances. Organic and inorganic compounds. *Ind. Engng Chem.* **39** (4), 517–540.

Tonini, S. & Cossali, G.E. 2015 A novel formulation of multi-component drop evaporation models for spray applications. *Intl J. Therm. Sci.* **89**, 245–253.

Tonini, S. & Cossali, G.E. 2016 One-dimensional analytical approach to modelling evaporation and heating of deformed drops. *Intl J. Heat Mass Transfer* **97**, 301–307.

Tonini, S. & Cossali, G.E. 2019 An analytical approach to model heating and evaporation of multicomponent ellipsoidal drops. *Heat Mass Transfer* **55** (5), 1257–1269.

Villermaux, E., Moutte, A., Amielh, M. & Meunier, P. 2017 Fine structure of the vapor field in evaporating dense sprays. *Phys. Rev. Fluids* **2** (7), 074501.

Wang, J., Dalla Barba, F. & Picano, F. 2021 Direct numerical simulation of an evaporating turbulent diluted jet-spray at moderate Reynolds number. *Intl J. Multiphase Flow* **137**, 103567.

Yarin, A.L., Brenn, G., Kastner, O., Rensink, D. & Tropea, C. 1999 Evaporation of acoustically levitated droplets. *J. Fluid Mech.* **399**, 151–204.